water

MDPI

Article

UV-Light-Driven Photocatalytic Dye Degradation and Antibacterial Potentials of Biosynthesized SiO_2 Nanoparticles

Parvathiraja Chelliah [1,*], Jeetendra Kumar Gupta [2], Saikh Mohammad Wabaidur [3], Masoom Raza Siddiqui [3], Siaw Foon Lee [4] and Wen-Cheng Lai [5,*]

[1] Department of Physics, Manonmaniam Sundaranar University, Tirunelveli 627012, India
[2] Institute of Pharmaceutical Research, GLA University, Mathura 281406, India
[3] Chemistry Department, College of Science, King Saud University, Riyadh 11451, Saudi Arabia
[4] The Eduardo Torroja Institute for Construction Sciences (IETcc—CSIC), 28033 Madrid, Spain
[5] Department of Electrical Engineering, Ming Chi University of Technology, New Taipei City 640243, Taiwan
* Correspondence: cpraja1206@gmail.com (P.C.); wenlai@mail.mcut.edu.tw or wenlai@mail.ntust.edu.tw (W.-C.L.)

Abstract: The present work shows the obtainment of biosynthesized SiO_2 with the aid of *Jasminum grandiflorum* plant extract and the study of its photocatalytic ability in dye degradation and antibacterial activity. The obtained biosynthesized SiO_2 nanoparticles were characterized using X-ray diffractometer analysis, Fourier transform infrared spectroscopy analysis, ultraviolet–visible diffuse reflectance spectroscopy, field-emission scanning electron microscope with energy-dispersive X-ray analysis, transmission electron microscopy and X-ray photoelectron spectroscopy. The UV-light irradiated photocatalytic activity of the biosynthesized SiO_2 nanoparticles was examined using methylene blue dye solution. Its reusability efficiency was determined over 20 cycles and compared with the commercial P-25 titanium dioxide. The bacterial resistivity of the biosynthesized SiO_2 nanoparticles was examined using *S. aureus* and *E. coli.* The biosynthesized SiO_2 nanoparticles showed a high level of crystallinity with no impurities, and they had an optimum crystallite size of 23 nm, a bandgap of 4 eV, no Si-OH groups and quasi-spherical shapes with Si-2p at 104 eV and O-1s at 533 eV. Their photocatalytic activity on methylene blue dye solution could reach 90% degradation after 40 min of UV light exposure, and their reusability efficiency was only 4% less than that of commercial P-25 titanium dioxide. At the concentration of 100 µg/mL, the biosynthesized SiO_2 nanoparticles could allow the resistivity of *E. coli* to become borderline to the resistant range of an antibiotic called Amikacin.

Keywords: SiO_2 nanoparticles; silicon; green synthesis; photocatalysis; *Jasminum grandiflorum*

Citation: Chelliah, P.; Gupta, J.K.; Mohammad Wabaidur, S.; Siddiqui, M.R.; Foon Lee, S.; Lai, W.-C. UV-Light-Driven Photocatalytic Dye Degradation and Antibacterial Potentials of Biosynthesized SiO_2 Nanoparticles. *Water* **2023**, *15*, 2973. https://doi.org/10.3390/w15162973

Academic Editor: William Frederick Ritter

Received: 20 July 2023
Revised: 8 August 2023
Accepted: 10 August 2023
Published: 18 August 2023

1. Introduction

Metal oxide nanoparticles are being used in diverse applications in various fields like drug delivery, absorbents, microbial activity, sensors, ceramics, catalysts, superconductors, semiconductors, superconductors, cancer activities, etc. [1–4]. Due to their wide bandgap, stability, low toxicity and high availability, metal oxides become highly used in several applications [5–9].

Metal oxide nanoparticles can be synthesized via different methods like green synthesis, sol–gel, co-precipitation, chemical/physical vapor deposition and hydrothermal methods [10–14]. Green synthesis is one of the best synthesis processes due to its lower toxicity, ease of use, low energy consumption and the fact that no secondary toxic compounds are composed in the synthesis time [14–17]. Moreover, by-products and unsuccessful synthesized products from green synthesis do not contribute to worldwide environmental water pollution [18–20].

In addition, pure water production is a process with many steps that has a high cost and requires high energy. The increase in population and industries is affecting pure water sources [20–22]. Most of the industries release dye onto land and into water systems, which

causes numerous problems for living beings [22–26]. Hence, scientists are taking serious actions to restore water systems and treat polluted water in the environment. Among all the water remediation processes, photocatalysis is one of the best and most efficient techniques in removing organic pollutants from wastewater systems. In addition, bacterial imperfections are a big threat to human health and can damage all nutrient systems. Therefore, currently, photocatalytic dye degradation techniques are highly needed worldwide [27].

When a photocatalyst is exposed to UV light, electron–hole pairs are produced as a result of the excitation of electrons from the valence band to the conduction band. This leads to redox reactions in which the reduction occurs in the conduction band and the oxidation occurs in the valence band. Thus, during photocatalysis, reactive oxygen species (ROS) such as hydroxyl radicals (•OH), superoxide radicals ($\bullet O_2$) and singlet oxygen ($^1O_2$) will be produced. These ROS will participate in chemical reactions that induce the degradation of organic pollutants adsorbed on the surface of the photocatalyst. For photocatalytic systems to operate at their best, it is essential to comprehend these chemical reactions properly [28–34].

It is reported that SiO_2 nanoparticles have high photocatalytic stability and endurance. Also, SiO_2 nanoparticles have high potential to produce reactive oxygen species (ROS) and enhance oxidative stress, which can produce the deduction of cell proliferation and suppress communications over the cell system [35,36]. The interface between Si and O atoms distributes electrons and forms encapsulation over the bio-elements.

The *Jasminum grandiflorum* plant comprises benzyl compounds, phytol compounds, linalool and eugenol that can assist in creating zero-valent metal atoms and lattice oxygen attachment [37–40].

Under UV light, biosynthesized SiO_2 nanoparticles that have bandgaps of 4 eV show good photocatalytic ability in MB dye degradation. On top of that, biosynthesized SiO_2 nanoparticles also provoke reactive oxygen species (ROS) and oxidative stress which can restrict cell viability. Thus, the current work focuses on two important aspects, which are (i) biosynthesized SiO_2 nanoparticles obtained from a mixture of *Jasminum grandiflorum* plant extract and sodium metasilicate nonahydrate and (ii) the methylene blue (MB) dye degradation and *S. aureus* and *E. coli* bacterial resistivity of nanomaterials.

2. Materials and Methods

2.1. Materials

Sodium metasilicate nonahydrate ($Na_2SiO_3 \cdot 9H_2O$, CAS number = 13517-24-3; 99.9% purity) and methylene blue dye ($C_{16}H_{18}ClN_3S \cdot 3H2O$, CAS number = 7220-79-3; 99.9% purity) were acquired from HiMedia, Mumbai, India. Jasminum grandiflorum plant flowers were collected from Kerala, India.

2.2. Preparation of Plant Extract

To obtain the plant extract, the Jasminum grandiflorum flowers were cleaned with running tap water in order to remove any dirt. The clean flowers (5 g) were then mixed with 100 mL of distilled water, and the mixture was heated at 70 °C for 10 min. The mixture was centrifuged at 10,000 rpm 3 times (with each time lasting 15 min) to separate the plant extract from the residue. The extract was then filtered with Whatman No. 1 filter paper (40 µm) to further remove the impurities. The obtained *Jasminum grandiflorum* extract was then used in the biosynthesis of SiO_2 nanoparticles. When it was not used straight away, it was stored in a refrigerator to prevent evaporation.

2.3. Biosynthesis of SiO_2 Nanoparticles

SiO_2 nanoparticles were synthesized using 0.1 M sodium metasilicate nonahydrate and 10 mL of *Jasminum grandiflorum* plant extract. These two solutions were mixed by using a magnetic stirrer for 30 min to obtain a milk-white solution. The white color provides information that Si^{4+} reduction took place, revealing the formation of SiO_2 nanoparticles in the solution. The white solution was centrifuged at 10,000 rpm three times (with each

time lasting 20 min) and then filtered with Whatman No. 1 filter paper (40 μm) to obtain the SiO_2 nanoparticles. The obtained pellets were heated in an oven at 100 °C for 2 h. The treated biosynthesized SiO_2 nanoparticles were then stored for the further evaluation of material characterizations.

2.4. Characterization of SiO_2 Nanoparticles

The material structure and phase stability were evaluated using an X-ray diffractometer (XRD) (PANalytical X'Pert with Cu Kα (1.5405 Å) in 30 kV and 40 mA). The optical properties were measured using ultraviolet–visible diffuse reflectance spectroscopy (UV-Vis DRS) (UV-2600 Shimadzu, Kyoto, Japan). The functional group of biosynthesized SiO_2 nanoparticles was evaluated using Fourier transform infrared spectroscopy (FTIR) (Perkin Elmer, Waltham, MA, USA; 4000 cm^{-1} to 400 cm^{-1}). The surface morphologies and their material presence were captured using a field-emission scanning electron microscope (FESEM) with energy-dispersive X-ray (EDX) analysis (Carl Zeiss, Jena, Germany) and a transmission electron microscope (TEM) (Titan, Hillsboro, OR, USA). The binding energies of the biosynthesized SiO_2 nanoparticles were observed using X-ray photoelectron spectroscopy (XPS, PHI 5000 Versa Probe III, Physical Electronics, Chanhassen, MN, USA). The determination of total organic carbon (TOC) values was carried out using a total organic carbon analyzer (TOC-VCPH/CPN, Shimadzu, Kyoto, Japan).

2.5. Photocatalytic Activity

The UV-light photocatalytic activity of the biosynthesized SiO_2 nanoparticles was examined using an MB dye solution (10 ppm). Then, 10 mg of SiO_2 nanoparticles was poured into the MB dye solution of 100 mL and the mixture was stirred for 40 min in the dark. The absence of light was used in order to achieve the adsorption–desorption equilibrium. The combined photocatalyst and dye solution was placed in a shielded chamber and exposed to the UV light source, which was a Deuterium lamp (λ = 160 nm). In the time interval of 10 min, an aliquot of 5 mL was taken out and centrifuged at 5000 rpm for 10 min to separate the catalyst from the dye solution. The obtained supernatant solution was pipetted out carefully and examined using UV–visible spectroscopy. The dye degradation due to the biosynthesized SiO_2 nanoparticle was then calculated [41,42]. The quenching experiment is an extremely helpful tool for determining the active species that are involved in the process of photocatalysis. These active species include superoxides, free radicals, sulphates and holes. In this study, quenchers with a concentration of 1 mmol/L were used for the analysis. These quenchers were triethanolamine (TEOA), p-benzoquinone (BQ), methanol (MeOH) and tert-butyl alcohol (TBA). The changes induced by these quenchers were measured using UV–visible spectroscopy, which provided insights into the role of the active species in the dye photodegradation.

2.6. Antibacterial Activity

The antibacterial resistivity of the biosynthesized SiO_2 nanoparticles was examined using a well diffusion method using Gram-positive *Staphylococcus aureus* (ATCC 6538) and Gram-negative *Escherichia coli* (ATCC 8739). The bacterial cultivation was carried out by injecting 10^{-6} CFU/mL into a nutrient broth. The loaded nutrient broth was then incubated for 12 h. The sterilized Petri plates composed of Mueller–Hinton agar were used by swabbing the incubated nutrient broth on it. The gel puncture was used to create a well that had a diameter of 5 mm. Different concentrations (10, 20, 50 and 100 μg/mL) of biosynthesized SiO_2 nanoparticles were put in the well. The sample-loaded Petri plates were incubated at 37 °C for the whole day. The inhibition zones of the biosynthesized SiO_2 nanoparticles with different concentrations were measured in mm scale. The bacterial activity of SiO_2 nanoparticles was compared with a standard antibiotic disc of Amikacin.

3. Result and Discussions

3.1. Biosynthesized SiO_2 Nanoparticles Reaction Mechanism

The possible mechanism (reduction and stabilization) involved in the synthesis of SiO_2 nanoparticles using the *Jasminum grandiflorum* plant extract could be explained as follows: The sodium silicate was used as a precursor, and the flower extract of *J. grandiflorum* was used as a reducing agent in the synthesis of SiO_2 nanoparticles. The chemical composition of the *Jasminum grandiflorum* plant is benzyl acetate (23.7%), benzyl benzoate (20.7%), phytol (10.9%), linalool (8.2%), isophytol (5.5%), phytyl acetate (5.3%) and volatile compounds which are linalool (3.0%), methyl linoleate (2.8%), eugenol (2.5%), cis-jasmone (1.9%), indole (1.8%), methyl palmitate (1.4%), benzyl alcohol (1.3%), α-farnesene (1.1%) and jasmine lactone (1.1%) [43]. Among those, the phytochemicals are benzyl acetate, phytol, isophytol, eugenol, linalool and oleuropein [43,44]. Herein, eugenol, which is a biologically active monoterpenoid, is reported to be involved in the biosynthesis of SiO_2 nanoparticles, acting as both a reducing and capping agent [45]. Similarly, in the present study, eugenol had a role as an electron donor which donated electrons to Si^{4+} ions to reduce them to SiO_2 nanoparticles and also stabilized the dissolved oxygen in the development of biosynthesized SiO_2 nanoparticles.

3.2. X-ray Diffraction Analysis

The X-ray diffraction pattern of the obtained biosynthesized SiO_2 nanoparticles is shown in Figure 1, and it is well-matched with a standard JCPDS card (46-1045) [46,47]. The broad peak at 20-32° corresponds to the (101) plane of SiO_2 nanoparticles in a hexagonal structure. The crystallite size of the biosynthesized SiO_2 nanoparticles was calculated using the Debye Scherrer formula [47–50], and the calculated optimum size is 23 nm. It can be seen that plant extract synthesis of silica method may produce SiO_2 nanoparticles with high crystallinity. In this work, the biosynthesized SiO_2 nanoparticles also exhibit high mitigation electron streams and refined crystalline properties. These properties of biosynthesized SiO_2 nanoparticles can lead to lattice strains as well as increasing charge separations. High crystallinity and the lower crystallite sizes of the biosynthesized SiO_2 nanoparticles are extremely important, especially in energy-, optical- and catalytic-related applications.

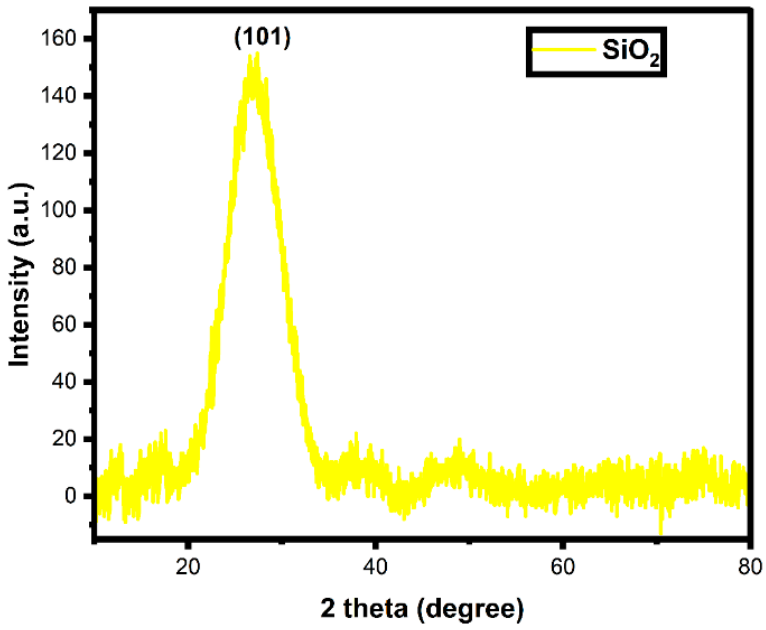

Figure 1. X-ray diffraction pattern of biosynthesized SiO_2 nanoparticles.

3.3. FTIR Analysis

The functional groups, surface modifications and purity of the plant extract and the biosynthesized SiO_2 nanoparticles were determined from FTIR spectroscopy (see Figure 2) with a limit of 400 to 4000 cm^{-1}. The FTIR analysis of the *Jasminum grandiflorum* plant extract exhibited distinctive peaks at 3313 cm^{-1}, 1619 cm^{-1} and 1029 cm^{-1}, showing the presence of particular functional groups in the extract. The peak at 3313 cm^{-1} indicates the presence of hydroxyl (OH) groups, which are likely attributable to substances such as benzyl acetate and eugenol, both of which have hydroxyl groups in their chemical structures [43]. Moreover, the presence of linalool, which contains hydroxyl groups, may also contribute to the observed peak at 3313 cm^{-1} [44]. The peak at 1619 cm^{-1} corresponds to the stretching vibrations of carbonyl (C=O) groups, indicating the presence of chemicals like benzyl acetate in the extract. The peak at 1029 cm^{-1} is associated with the C-O bond's bending vibration that coincides with the presence of substances like phytol, isophytol and oleuropein, all of which have either groups or alcohol moieties in their structures. These FTIR results corroborate the presence of the compounds such as benzyl acetate, phytol, isophytol, eugenol, linalool, and oleuropein in the extract. As for the biosynthesized SiO_2 nanoparticles, the vibration bands around 460 cm^{-1} and 1099 cm^{-1} are due to the bending and asymmetric vibrations of Si–O and Si–O–Si [51]. Similarly, the band around 813 cm^{-1} is caused by the symmetric vibrations of Si–O–Si. No broad band is near 3440 cm^{-1}, which corresponds to O-H stretching due to Si-OH vibration or surface-absorbed water molecules by silica moieties [52,53]. The obtained FTIR spectra of the biosynthesized SiO_2 nanoparticles were compared with the previous literature, and there are no additional peaks appearing in the FTIR spectra, which would indicate the presence of any impurities. Plant molecules assist in producing Si^{4+} to O^{2-} ions and stabilizing the ions in the biosynthesis of SiO_2 nanoparticles [54–58].

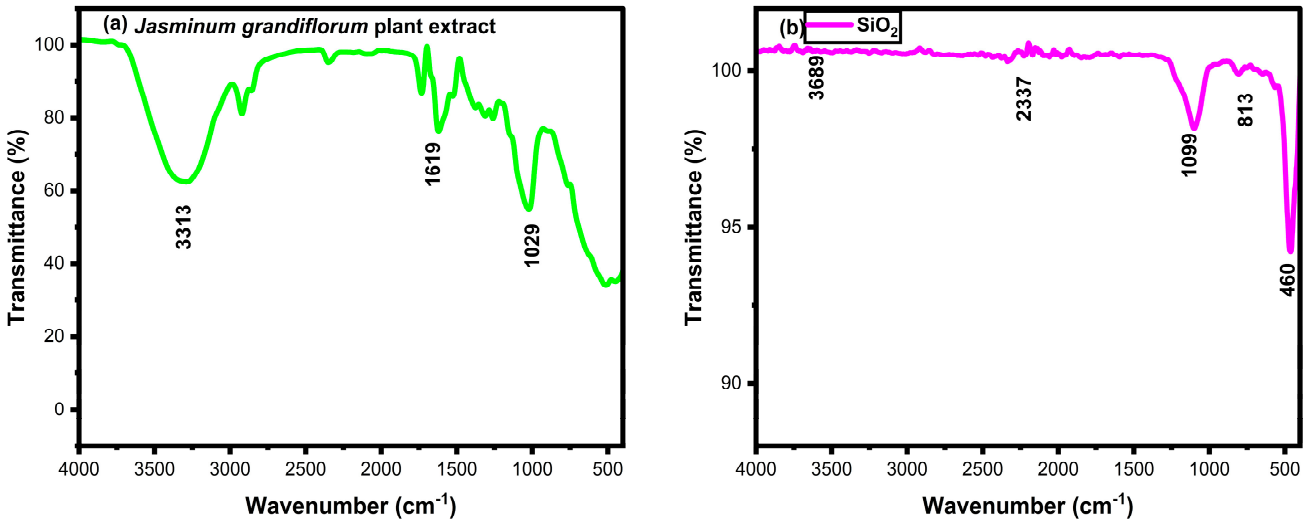

Figure 2. FTIR spectra of (**a**) *Jasminum grandiflorum* plant extract and (**b**) biosynthesized SiO_2 nanoparticles.

3.4. UV-Vis DRS Analysis

The optical properties of biosynthesized SiO_2 were collected from the UV-Vis DRS. The absorbance spectrum of the biosynthesized SiO_2 nanoparticles is shown in Figure 3a. The Kubelka–Munk relationship was used to find the bandgap value of the biosynthesized SiO_2 nanoparticles, as shown in Figure 3b. Tracing the slope to the x-axis of the absorbance spectrum in Figure 3a, the wavelength is found to be around 310 nm, which is similar to the bandgap value of 4 eV, as shown in Figure 3b.

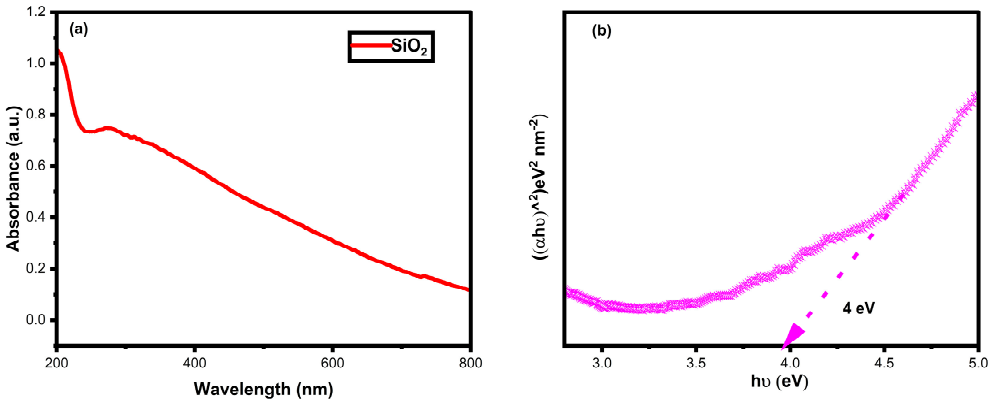

Figure 3. (**a**) UV-DRS absorbance spectrum and (**b**) bandgap spectrum of biosynthesized SiO_2 nanoparticles.

3.5. FESEM with EDX Analysis

Figure 4a–d depict the structure and the material state of the biosynthesized SiO_2 nanoparticles. Quasi-spherical and conjoint-spherical shapes are observed in the biosynthesized SiO_2 nanoparticles, and an agglomeration of particles can be seen in Figure 4a,b. The EDX spectrum and the weight percent of Si and O atoms are presented in Figures 4c and 4d, respectively. The weight percent of Si atoms is half of that of O atoms, which is shown in Figure 4d. The oxygen orientation and the metal element reduce the degree of agglomeration and increase stability. Moreover, the oxygen enrichment in the biosynthesized SiO_2 nanoparticles could induce electron trapping in dye degradation and bacterial inactivation activities. In addition, the *Jasminum grandiflorum* plant extract ensures the formation of SiO_2 nanoparticles in the biosynthesis [59–61]. Furthermore, the biosynthesized SiO_2 nanoparticles are highly acceptable nanoparticles in bacterial- and water-remediation-related applications.

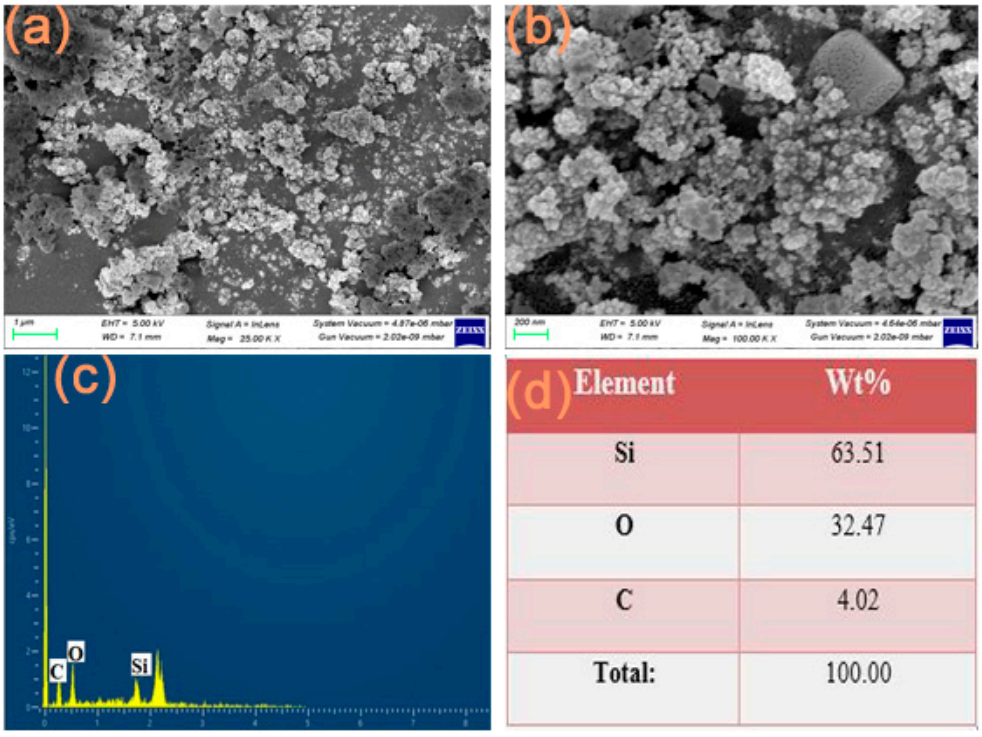

Figure 4. (**a**,**b**) FESEM images under two different magnifications and (**c**,**d**) EDX spectrum and table of biosynthesized SiO_2 nanoparticles.

3.6. TEM Analysis

The morphological entity and the size of the biosynthesized SiO_2 nanoparticles were detected using transmission electron microscopy. Figure 5a,b display the TEM images of the biosynthesized SiO_2 nanoparticles having quasi-spherical and conjoint-spherical shapes, which is consistent with Figure 4a,b. The magnification of the biosynthesized SiO_2 nanoparticles at 100 nm clearly depicts poly-dispersive and equally distributed quasi-spherical shapes. The higher magnification at 50 nm on a different spot also demonstrates conjoint-spherical shapes [62–65].

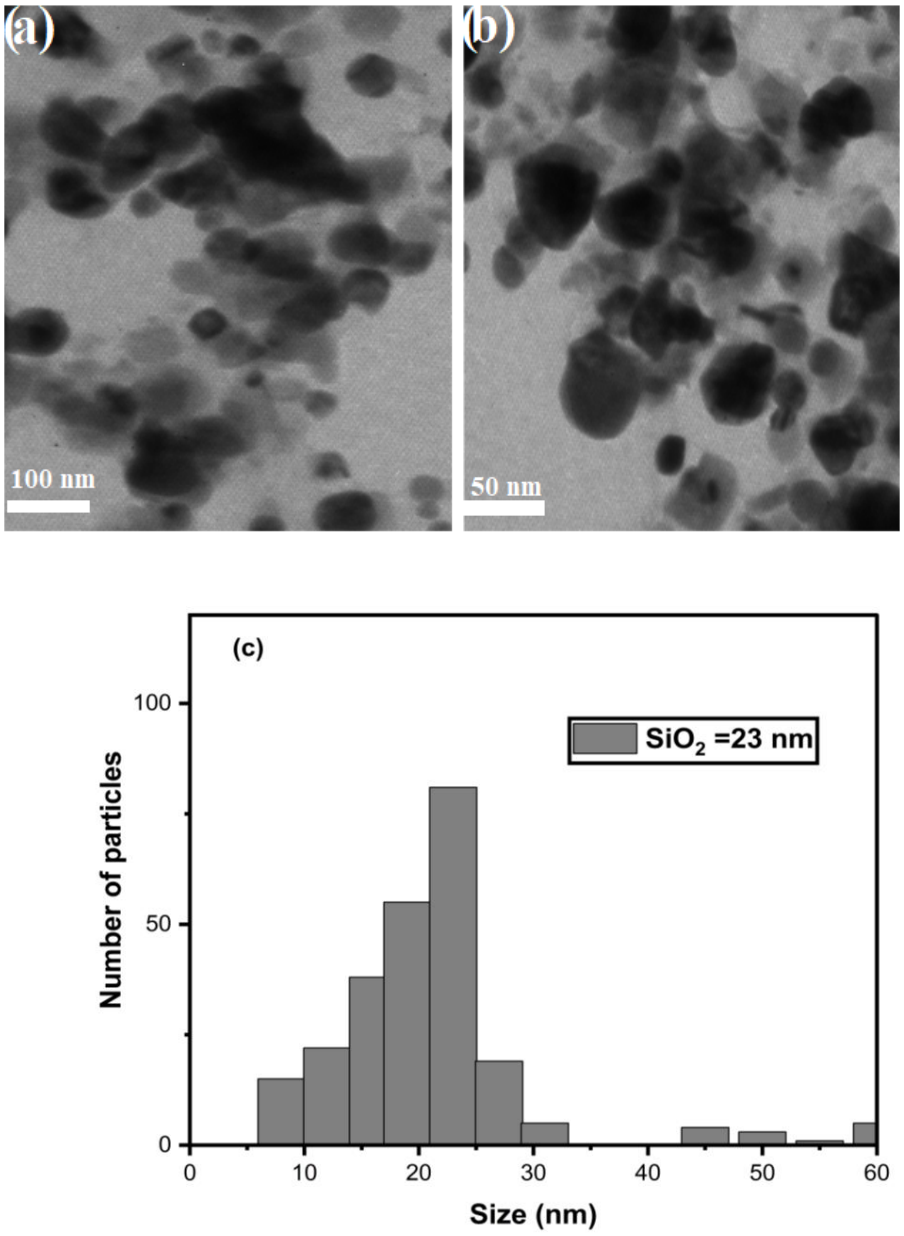

Figure 5. (**a**,**b**) TEM images of biosynthesized SiO_2 nanoparticles under two different magnifications. (**c**) Histogram of the number of particles of biosynthesized SiO_2 nanoparticles versus size.

The histogram of SiO_2 nanoparticles was plotted from the TEM images using ImageJ software version 1.44; see Figure 5c. It can be seen that the biosynthesized SiO_2 nanoparticles show various sizes; however, their distribution is high in the range of 10–28 nm in size. Larger particles with sizes between 43 and 60 nm can be seen also in Figure 5c, but their quantities are a lot lower. The obtained optimum size with the highest number of

particles is around 23 nm, which is well matched with the XRD crystallite size obtained in Section 3.2.

3.7. XPS Analysis

The binding energy spectra of the biosynthesized SiO_2 nanoparticles obtained from X-ray photoelectron spectroscopy are shown in Figure 6. The wide spectrum in Figure 6a reveals the presence of Si and O and C elements. The carbon peaks which are composed of C-C, C-O, C-H and C=O in Figure 6d are mainly due to the contamination of the environmental air because XRP is a quantitative technique that is very surface sensitive. The detailed scan of a Si atom in the SiO_2 nanoparticles is located at 104 eV, revealing the Si-2p state [66,67]. The O-1s peak located at 533 eV reveals the lattice oxygen that is attached to the Si-2p state. The findings show that the biosynthesized SiO_2 nanoparticles are free of impurities.

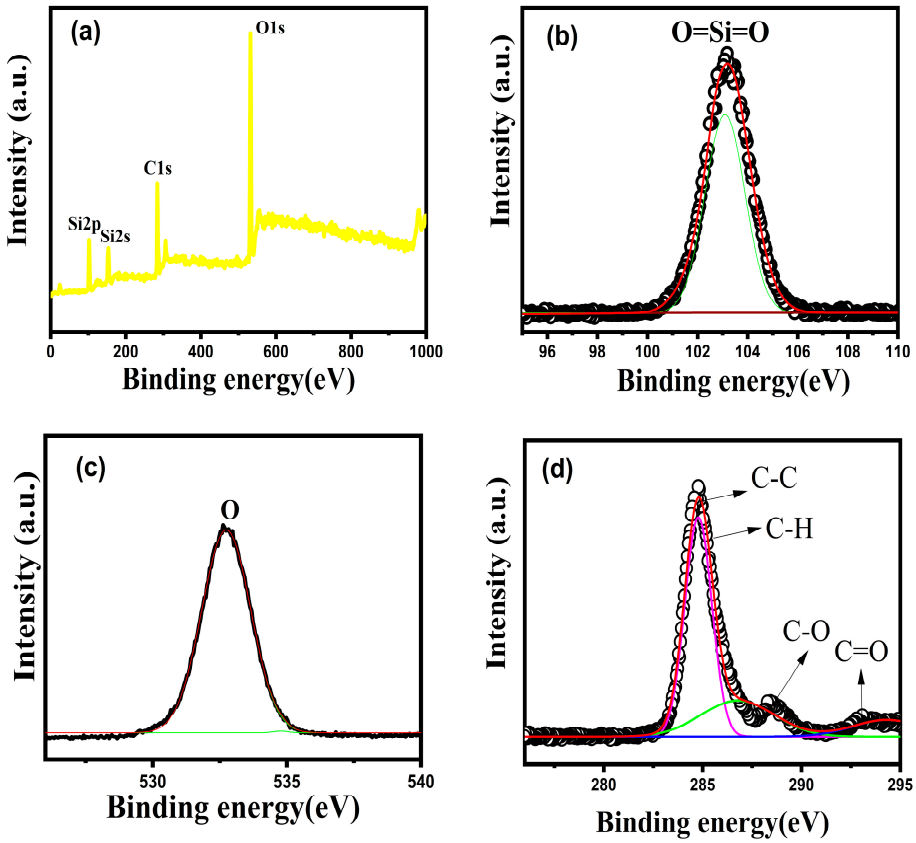

Figure 6. (**a**) A full scan of XPS, (**b**) Si, (**c**) O and (**d**) C spectra of biosynthesized SiO_2 nanoparticles.

3.8. Photocatalytic Dye Degradation

In this study, an MB dye was used to determine the photocatalytic potential of the biosynthesized SiO_2 nanoparticles under UV-light irradiation. The degradation analysis was carried out on an aliquot in the time interval of 10 min for a duration of 40 min. The absorbance spectra of the MB photodegradation with the biosynthesized SiO_2 nanoparticles is shown in Figure 7a, the degradation percentage in Figure 7b and the pseudo-first-order reaction rate constant in Figure 7c. The UV-light irradiation over the dye and catalyst solution excites the electrons from the valence band to the conduction band of the biosynthesized SiO_2 nanoparticles. The photoexcited electrons on the conduction band are captured by the dissolved O_2 molecules, which are then turned into superoxide radical anions ($O_2^{\bullet -}$) [68–72]. The reduction of $O_2^{\bullet -}$ will turn it into hydrogen peroxide (H_2O_2). The further reduction of (H_2O_2) will turn it into hydroxyl radical ($OH^{\bullet}$), which will degrade the MB dye solution. On the other hand, the MB dye solution can also

undergo degradation with holes at the valence band. The color of the MB dye solution gradually becomes less intense when the reaction proceeds on the surface of the biosynthesized SiO_2 nanoparticles. On top of that, UV-light irradiation can also degrade the dye molecules due to their photolysis effect. The degradation percent of the MB dye solution without the biosynthesized SiO_2 nanoparticles under UV light is found to be 16%, which is demonstrated in Figure 7b. The degradation of the MB dye solution on the surface of the biosynthesized SiO_2 nanoparticles can reach 90% after 40 min at a kinetic constant of 0.04704 min^{-1}. The equations starting from the electrons being excited under UV light on the surface of the biosynthesized SiO_2 nanoparticle until the MB dye's degradation are described as follows:

$$SiO_2 + h\nu \rightarrow h^+_{VB} + e^-_{CB}$$

$$O_2 + e^-_{CB} \rightarrow O_2^{\bullet -}$$

$$O_2^{\bullet -} + e^-_{CB} + 2H^+ \rightarrow H_2O_2$$

$$H_2O_2 + e^-_{CB} + H^+ \rightarrow HO^{\bullet} + H_2O$$

$$\text{MB} + OH^{\bullet} \rightarrow CO_2 + H_2O$$

$$\text{MB} + h^+_{VB} \rightarrow MB^{\bullet +}(intermediate) \rightarrow oxidation\ of\ MB$$

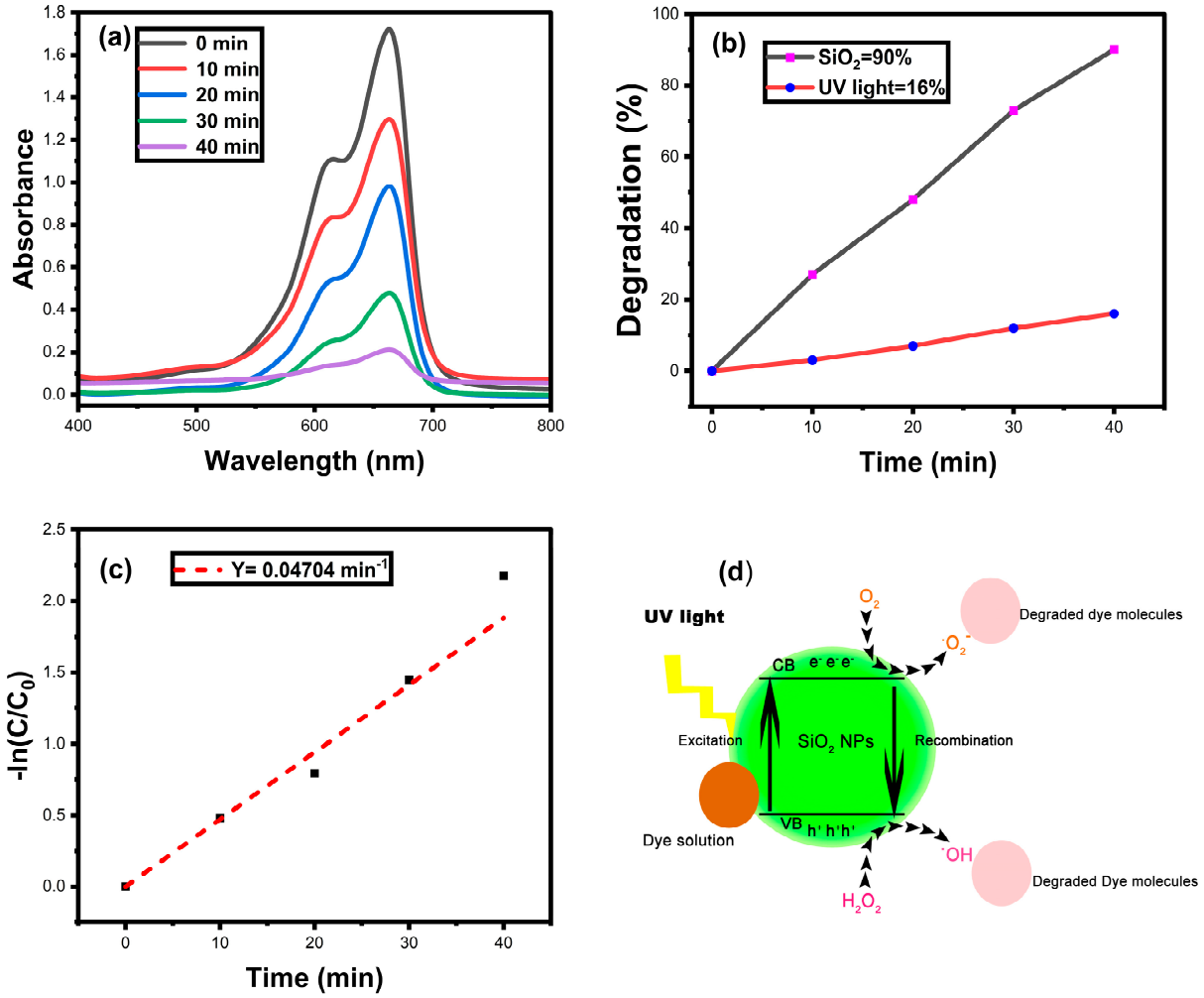

Figure 7. (**a**) Absorbance of photodegradation of MB, (**b**) degradation percentage, (**c**) pseudo-first-order kinetic rate constant and (**d**) MB degradation mechanism on biosynthesized SiO_2 nanoparticles.

The degradation of hazardous organic substances on semiconductor nanoparticles is basically influenced by three important parameters: (i) electron excitation and empty hole creation during irradiation, (ii) superoxide and hydroxyl radical generation and (iii) organic pollutant degradation [71–73]. The biosynthesized SiO_2 nanoparticles provide the central electric ground, with charge separation being induced by UV light [69–73]. The charge separation will then lead to the hydroxyl radical generation that promotes the degradation activity in the dye compounds [74,75]. A schematic drawing of the dye photodegradation mechanism is depicted in Figure 7d.

Reusability Analysis

Industrial-scale photocatalysts are mainly based on the durability and efficiency of the photocatalytic materials. The recycling efficiency of the biosynthesized SiO_2 nanoparticles is compared with the P-25 titanium dioxide up to 20 cycles, as displayed in Figure 8. The initial degradation percentage is 90% of SiO_2 and 96% of P-25. It can be seen that the degradation percent decreases slowly every five cycles. In the 20th cycle, the degradation percentage of SiO_2 becomes 86% and that of P-25 becomes 91%. The degradation difference is 4% between the SiO_2 and P-25 photocatalysts. This shows that the biosynthesized SiO_2 nanoparticles are actively equal to the commercial P-25 photocatalyst. Degradation losses can be caused by various factors such as (i) the usage of the surface (dry and wash), (ii) active sites being covered by targeted materials and (iii) the whole surface and pores being blocked by secondary products. This work shows that the stability of the biosynthesized SiO_2 nanoparticles is high and their degradation losses are minimal. All these factors indicate that they could be used as a good photocatalyst against pollutants because their reusability is more or less equal to the commercial P-25 photocatalyst.

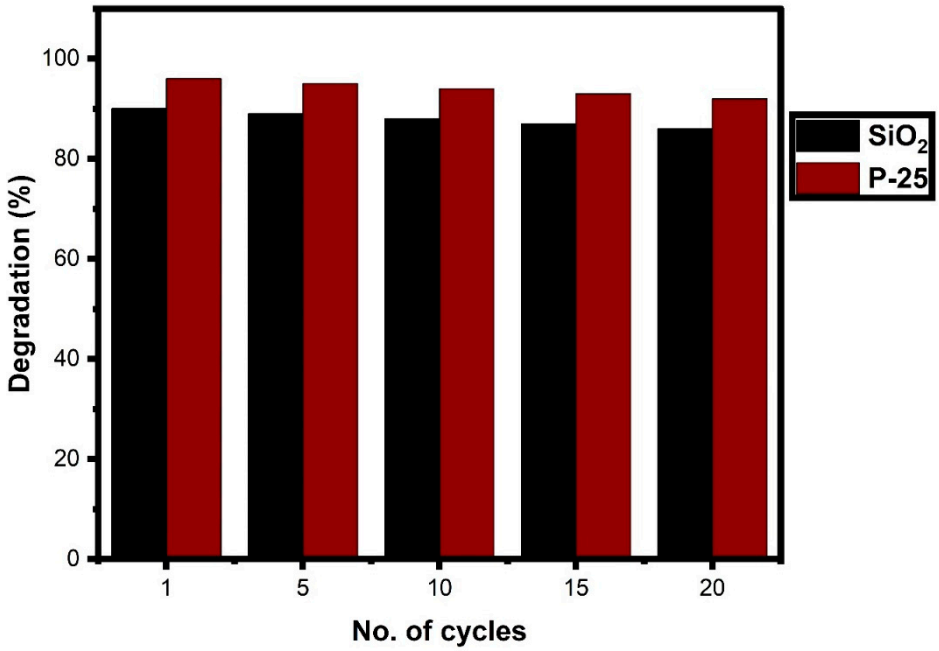

Figure 8. Reusability study of biosynthesized SiO_2 nanoparticles.

Photocatalysis is influenced by various parameters like dye volume, the irradiation of the light source, the catalyst dosage and the bandgap of the materials. In this study, the photocatalytic activity of the biosynthesized SiO_2 nanoparticles is compared with the previously reported SiO_2 associated with other metal oxides are tabulated in Table 1. The metal–oxide interface reduces the electron–hole recombination and prolongs the lifetime, which induces the degradation activity [76,77]. Noble metal association on the SiO_2 nanoparticles increases the metal trap on the catalyst surface which could increase the degradation potential [76,78]. The reported ZnO@SiO_2-Ag nanoparticles reduced MB

dye by 81% when exposed to visible light, while TiO_2@SiO_2-Ag nanoparticles reduced Rh-B dye by 92% and MB dye by 85% when exposed to visible light. With the sunlight as a light source, MB dye was reduced by 97.7% in core–shell SiO_2/TiO_2 nanoparticles. Noble metal–carbon decorations of SiO_2 nanoparticles accelerated the electron excitation and improved the oxidation and reduction capabilities of the catalyst; thus, they can produce better photocatalytic degradation against various dyes [78–87]. The dopant of SiO_2 nanoparticles encourages a high adsorption ability compared to pure SiO_2 nanoparticles. Due to their wide bandgap, SiO_2 nanoparticles cannot absorb visible light, and thus, they need some dopants to help absorb visible light. UV-light irradiation motivated charge carriers and produced high active OH radicals on pure SiO_2 nanoparticles that had large surface areas, high porosity levels and different crystalline natures, allowing them to have good degradation efficiency against the noxious dye compounds.

Table 1. Photocatalytic comparison table of reported SiO_2 associated with other metal oxides to biosynthesized SiO_2 nanoparticles in this study.

S.no	Sample	Dye	Light Source	Dosage	Dye Volume	Degradation Percentage	Ref
1.	ZnO@SiO_2-Ag	MB	Visible light	0.1 g	100 mL	81	[76]
2.	TiO_2@SiO_2-Ag	Rh-B and MB	Visible light	100 mg	100 mL	92 and 85	[77]
3.	Core–shell SiO_2/TiO_2	MB	Sun light	10 mg	100 mL	97.7	[88]
4.	Nitrogen-doped SiO_2/TiO_2	MB	Visible light	0.010 g	20 mL	96	[79]
5.	Zn-doped-SiO_2	CV	Solar light	0.5 mg	100 mL	85.5	[80]
6.	CeO_2-SiO_2	Rhodamine 6G	Visible light	5 mg	5 mL	98	[81]
7.	Ag-modified hollow SiO_2/TiO_2	Rh-B	Visible light	30 mg	50 mL	90	[82]
8.	Graphene/SiO_2	MO	UV light	0.03g	100 mL	99	[78]
9.	Ag_2CrO_4 over SiO_2-aerogel	ORGANIC DYE	Visible light	0.2 g	100 mL	95.4	[83]
10.	g-C_3N_4/SiO_2-Au	Rh-B	Visible light	0.05 g	50 mL	99.8	[84]
11.	TiO_2/SiO_2	cationic blue X-GRL	UV light	0.08 g	50 mL	95	[85]
12.	$Pb_3Nb_4O_{13}$/fumed SiO_2	Rhodamine B	Visible light	0.3 g	100 mL	96	[86]
13.	Nd_2O_3-SiO_2	MV	UV light	120 mg	50 mL	95	[87]
14.	**SiO_2**	**MB**	**UV light**	**10 mg**	**100 mL**	**90**	**Present work**

The presence of sulphates, holes, superoxides and hydroxide radicals can have a significant impact on how effectively the process of photocatalytic degradation works. The findings of the experiment on quenching are presented in Figure 9, which shows the percentage of degradation without the use of quenchers is 90%. It is possible to draw parallels between this value and the suppression values of holes, superoxides and hydroxides. Hydroxides, superoxides and holes all have higher suppression values than MeOH, as shown in the figure. It is clear that the resistance of holes to degradation is superior to that of hydroxides and superoxides, and their association with the photocatalyst boosts the activity of the photocatalyst when it comes to the degradation of dye. The biosynthesized SiO_2 nanoparticles have a high capacity for absorption and make a significant contribution to the degradation process; as a result, the efficiency of the process is significantly improved.

These findings shed light on the possibility that the biosynthesized SiO_2 nanoparticles could improve the efficiency of photocatalytic dye degradation.

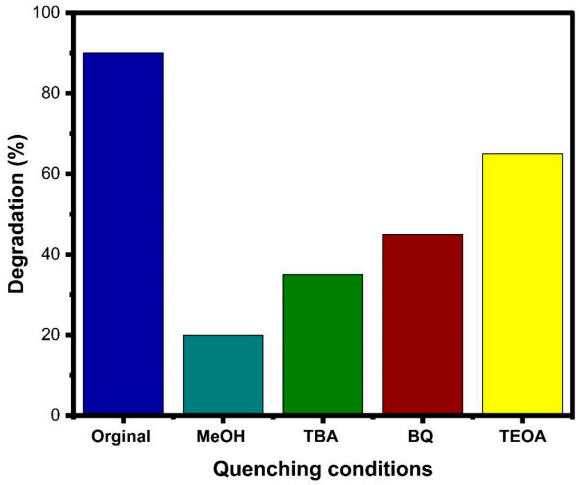

Figure 9. Quenching analysis of biosynthesized SiO_2 nanoparticles.

The efficiency with which a SiO_2 photocatalyst mineralized substances was determined via total organic carbon (TOC) analysis. The efficiency of the biosynthesized SiO_2 photocatalyst in terms of %TOC removal is displayed in Figure 10. Only 5% of the organic species are converted to minerals in the first 10 min. However, after 60 min, that percentage rises to 30.0%, and after 120 min, it rises to 65.0%. The remaining organic molecules in the MB dye are successfully converted to inorganic minerals using the UV/SiO_2 nanoparticle system, as demonstrated by these results. This suggests that the biosynthesized SiO_2 photocatalyst could be used to degrade and transform organic pollutants, as the efficiency of mineralization increases over time.

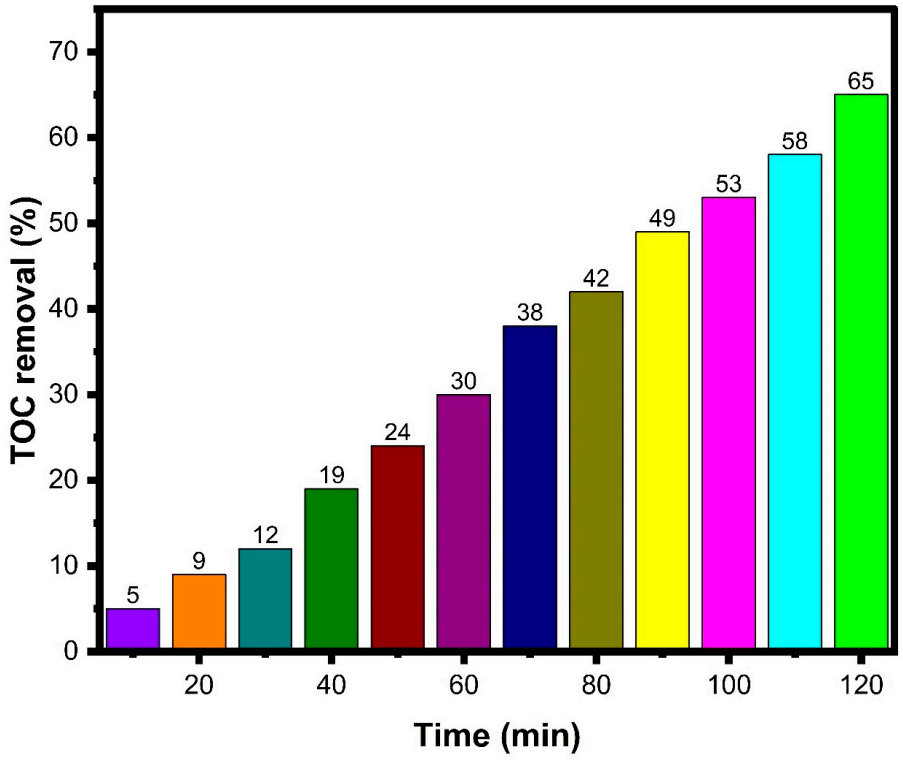

Figure 10. TOC analysis of biosynthesized SiO_2 nanoparticles.

3.9. Antibacterial Activity

The zone of inhibitions of the biosynthesized SiO_2 nanoparticles with different concentrations against the bacterial activities of *E. coli* and *S. aureus* is presented in Figure 9. In general, it can be seen that the zone of inhibitions increases when the concentration of biosynthesized SiO_2 nanoparticles increases for both types of bacteria. Closely examining the histogram, at the concentrations below 20 µg/mL, Gram-negative *E. coli* exhibits higher bacterial activity than Gram-positive *S. aureus*. At a concentration higher than 50 µg/mL, Gram-negative *E. coli* exhibits less bacterial activity than Gram-positive *S. aureus*. Compared to the zone inhibition diameter of the control, Amikacin, in Table 2, Gram-negative *E. coli* starts to lose its resistivity at the concentration of 100 µg/mL as the achieved zone of inhibition is 14 mm, which is at the border of the resistant range. However, *S. aureus* still has strong resistivity against the concentration of 100 µg/mL because the achieved zone of inhibition is 11 mm. Biosynthesized SiO_2 nanoparticles and dissolved oxygen gas can lead to the generation of various ROS. The antibacterial mechanism of biosynthesized SiO_2 nanoparticles is explained in Figure 11. The bacterial interface undergoes dissociation with metal ions, which plays a key role in bacterial inactivation activities. Abundant reports demonstrate the probable mechanism of the antibacterial activity of nanoparticles [89–94]. The present work discusses the bacterial inactivation mechanism against the bacterial strain and compares it with the previous literature. The Si^{4+} efficiently interacts with the charged bacterial strain surface and breaks down the body of the membrane's operational outline [95,96]. Moreover, Si^{4+} damages the cell membrane assembly, and subsequently, it may promote cell deactivations. Further, Figure 12 shows that Si^{4+} and O^{2-} ions' dissolution together with ROS development can result in the deactivation of bio-compounds and provoke cell death.

Table 2. Inhibition zone diameter of Amikacin as control.

Control	Zone Diameter According to the Criteria Published CLSI [95]		
	Resistant (mm)	**Intermediate (mm)**	**Susceptible (mm)**
Amikacin	≤14	15–16	≥17

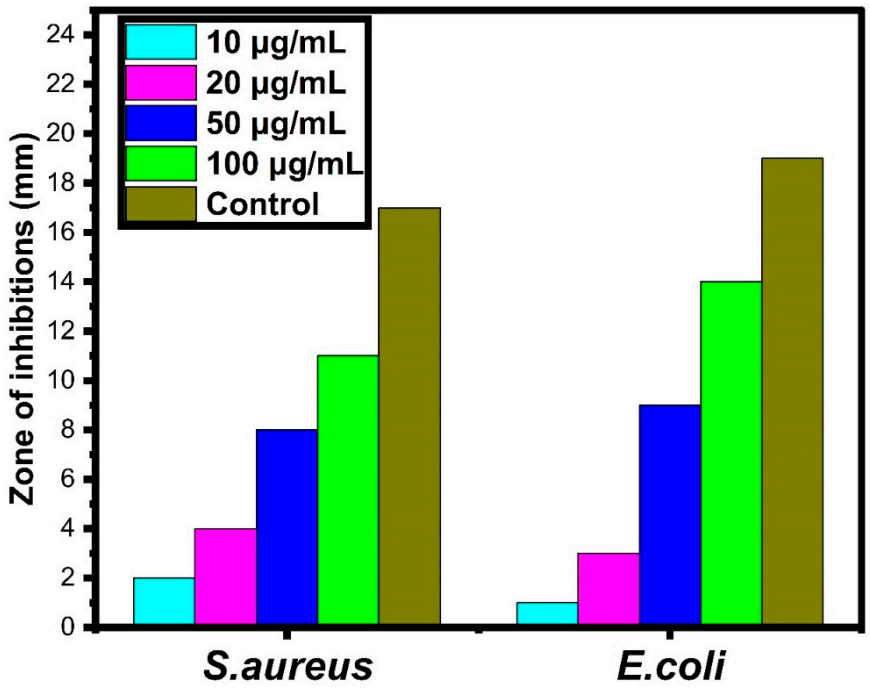

Figure 11. Antibacterial activity of biosynthesized SiO_2 nanoparticles.

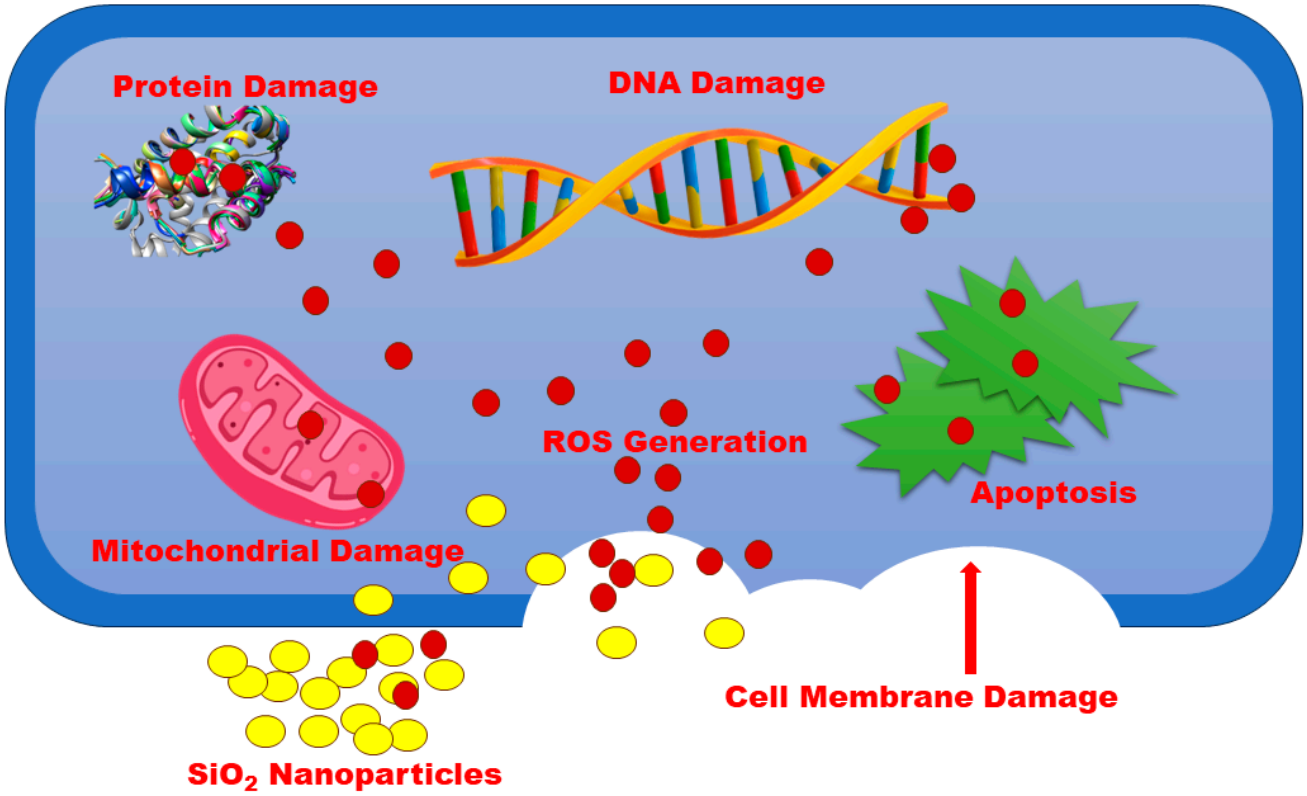

Figure 12. Antibacterial mechanism of biosynthesized SiO_2 nanoparticles.

4. Conclusions

The biogenic production of nanomaterials mainly focuses on decreasing the chemical use and increasing the chemical-free environment. In this study, biosynthesized SiO_2 nanoparticles were successfully synthesized from a mixture of *Jasminum grandiflorum* plant extract and sodium metasilicate nonahydrate. The biosynthesized SiO_2 nanoparticles could produce reactive oxygen species that would lead to antibacterial activity in the bacterial systems. The MB dye degradation of SiO_2 is 90% after 40 min under UV-light irradiation, and *E.coli* has less resistivity than *S. aureus* at the concentration of 100 µg/mL of biosynthesized SiO_2 nanoparticles. As a result, the biosynthesized SiO_2 nanoparticles could be used as substitutes for water purification and bacterial elimination.

Author Contributions: Conceptualization, P.C., S.M.W., S.F.L. and W.-C.L.; methodology, P.C. and W.-C.L.; software, P.C.; validation, P.C., J.K.G., S.F.L. and W.-C.L.; formal analysis, P.C. and S.F.L.; investigation, P.C., J.K.G. and W.-C.L.; resources, S.M.W. and W.-C.L.; data curation, P.C., S.M.W., J.K.G. and W.-C.L.; writing—original draft, P.C.; writing—review and editing, P.C., S.M.W. and S.F.L.; visualization, P.C.; supervision, S.M.W., S.F.L. and W.-C.L.; project administration, S.M.W. and W.-C.L.; funding acquisition, S.M.W., M.R.S., S.F.L. and W.-C.L. All authors have read and agreed to the published version of the manuscript.

Funding: Authors are grateful to the Researchers Supporting Project No. (RSP2023R326), King Saud University, Riyadh, Saudi Arabia.

Data Availability Statement: All research data associated with the manuscript are available.

Acknowledgments: The authors are grateful to the Researchers Supporting Project No. (RSP2023R326), King Saud University, Riyadh, Saudi Arabia. Parvathiraja Chelliah is thankful to the V.O. Chidambaram College, Thoothukudi, Tamilnadu and Sadakathullah Appa College, Tirunelveli, Tamilnadu, India.

Conflicts of Interest: The authors have no conflict of interest.

References

1. Li, T.; Yin, W.; Gao, S.; Sun, Y.; Xu, P.; Wu, S.; Kong, H.; Yang, G.; Wei, G. The combination of two-dimensional nanomaterials with metal oxide nanoparticles for gas sensors: A review. *Nanomaterials* **2022**, *12*, 982. [CrossRef] [PubMed]
2. Jeevanandam, J.; Kiew, S.F.; Boakye-Ansah, S.; Lau, S.Y.; Barhoum, A.; Danquah, M.K.; Rodrigues, J. Green approaches for the synthesis of metal and metal oxide nanoparticles using microbial and plant extracts. *Nanoscale* **2022**, *14*, 2534–2571. [CrossRef] [PubMed]
3. Patil, S.P.; Chaudhari, R.Y.; Nemade, M.S. Azadirachta indica leaves mediated green synthesis of metal oxide nanoparticles: A review. *Talanta Open* **2022**, *5*, 100083. [CrossRef]
4. Karlsson, H.L.; Toprak, M.S.; Fadeel, B. Toxicity of metal and metal oxide nanoparticles. In *Handbook on the Toxicology of Metals*; Academic Press: London, UK, 2022; pp. 87–126.
5. Roy, A.; Murthy, H.A.; Ahmed, H.M.; Islam, M.N.; Prasad, R. Phytogenic synthesis of metal/metal oxide nanoparticles for degradation of dyes. *J. Renew. Mater.* **2022**, *10*, 1911–1930. [CrossRef]
6. Lv, Z.; Zhang, J.; Zhang, Y.; Li, K.; Ye, X.; Fang, M.; Tan, X.; Kong, M.; Wang, X. Selective and efficient removal of radioactive ions from water with well-dispersed metal oxide nanoparticles@N-doped carbon. *Sep. Purif. Technol.* **2022**, *285*, 120366. [CrossRef]
7. Kalia, A.; Kaur, J.; Kaur, A.; Singh, N. Antimycotic activity of biogenically synthesised metal and metal oxide nanoparticles against plant pathogenic fungus *Fusarium moniliforme* (*F. fujikuroi*). *Indian J. Exp. Biol. (IJEB)* **2022**, *58*, 263–270.
8. Kundu, C.K.; Song, L.; Hu, Y. Chitosan-metal oxide nanoparticle hybrids in developing bi-functional polyamide 66 textiles with enhanced flame retardancy and wettability. *Appl. Surf. Sci. Adv.* **2022**, *7*, 100202. [CrossRef]
9. Alavi, M.; Rai, M.; Martinez, F.; Kahrizi, D.; Khan, H.; Rose Alencar De Menezes, I.; Coutinho, H.D.M.; Costa, J.G.M. The efficiency of metal, metal oxide, and metalloid nanoparticles against cancer cells and bacterial pathogens: Different mechanisms of action. *Cell. Mol. Biomed. Rep.* **2022**, *2*, 10–21. [CrossRef]
10. Bustamante-Torres, M.; Romero-Fierro, D.; Estrella-Nuñez, J.; Arcentales-Vera, B.; Chichande-Proaño, E.; Bucio, E. Polymeric composite of magnetite iron oxide nanoparticles and their application in biomedicine: A review. *Polymers* **2022**, *14*, 752. [CrossRef]
11. Hammad, E.N.; Salem, S.S.; Mohamed, A.A.; El-Dougdoug, W. Environmental impacts of ecofriendly iron oxide nanoparticles on dyes removal and antibacterial activity. *Appl. Biochem. Biotechnol.* **2022**, *194*, 6053–6067. [CrossRef]
12. Wang, H.; Biswas, P.; Zachariah, M.R. Direct Imaging and Simulation of the Interface Reaction of Metal/Metal Oxide Nanoparticle Laminates. *J. Phys. Chem. C* **2022**, *126*, 8684–8691. [CrossRef]
13. Kumar, P.; Tomar, V.; Kumar, D.; Joshi, R.K.; Nemiwal, M. Magnetically active iron oxide nanoparticles for catalysis of organic transformations: A review. *Tetrahedron* **2022**, *106–107*, 132641. [CrossRef]
14. Mabrouk, M.; Ibrahim Fouad, G.; El-Sayed, S.A.; Rizk, M.Z.; Beherei, H.H. Hepatotoxic and neurotoxic potential of iron oxide nanoparticles in Wistar rats: A biochemical and ultrastructural study. *Biol. Trace Elem. Res.* **2022**, *200*, 3638–3665. [CrossRef] [PubMed]
15. Sardar, M.; Ahmed, W.; Al Ayoubi, S.; Nisa, S.; Bibi, Y.; Sabir, M.; Khan, M.M.; Ahmed, W.; Qayyum, A. Fungicidal synergistic effect of biogenically synthesized zinc oxide and copper oxide nanoparticles against *Alternaria citri* causing citrus black rot disease. *Saudi J. Biol. Sci.* **2022**, *29*, 88–95. [CrossRef]
16. Fouda, A.; Eid, A.M.; Abdel-Rahman, M.A.; El-Belely, E.F.; Awad, M.A.; Hassan, S.E.D.; Al-Faifi, Z.E.; Hamza, M.F. Enhanced antimicrobial, cytotoxicity, larvicidal, and repellence activities of brown algae, *Cystoseira crinita*-mediated green synthesis of magnesium oxide nanoparticles. *Front. Bioeng. Biotechnol.* **2022**, *10*, 849921. [CrossRef]
17. Abdelmigid, H.M.; Hussien, N.A.; Alyamani, A.A.; Morsi, M.M.; AlSufyani, N.M.; Kadi, H.A. Green Synthesis of Zinc Oxide Nanoparticles Using Pomegranate Fruit Peel and Solid Coffee Grounds vs. Chemical Method of Synthesis, with Their Biocompatibility and Antibacterial Properties Investigation. *Molecules* **2022**, *27*, 1236. [CrossRef]
18. Tang, W.; Pei, Y.; Zheng, H.; Zhao, Y.; Shu, L.; Zhang, H. Twenty years of China's water pollution control: Experiences and challenges. *Chemosphere* **2022**, *295*, 133875. [CrossRef] [PubMed]
19. Xue, J.; Wang, Q.; Zhang, M. A review of non-point source water pollution modeling for the urban–rural transitional areas of China: Research status and prospect. *Sci. Total Environ.* **2022**, *826*, 154146. [CrossRef] [PubMed]
20. Mumbi, A.W.; Watanabe, T. Cost Estimations of Water Pollution for the Adoption of Suitable Water Treatment Technology. *Sustainability* **2022**, *14*, 649. [CrossRef]
21. Haghnazar, H.; Cunningham, J.A.; Kumar, V.; Aghayani, E.; Mehraein, M. COVID-19 and urban rivers: Effects of lockdown period on surface water pollution and quality-a case study of the Zarjoub River, north of Iran. *Environ. Sci. Pollut. Res.* **2022**, *29*, 27382–27398. [CrossRef]
22. Huang, Y.; Mi, F.; Wang, J.; Yang, X.; Yu, T. Water pollution incidents and their influencing factors in China during the past 20 years. *Environ. Monit. Assess.* **2022**, *194*, 182. [CrossRef] [PubMed]
23. Tabrez, S.; Zughaibi, T.A.; Javed, M. Water quality index, *Labeo rohita*, and *Eichhornia crassipes*: Suitable bio-indicators of river water pollution. *Saudi J. Biol. Sci.* **2022**, *29*, 75–82. [CrossRef] [PubMed]
24. Zhang, J.; Li, H.; Jiao, G.; Wang, J.; Li, J.; Li, M.; Jiang, H. Spatial Pattern of Technological Innovation in the Yangtze River Delta Region and Its Impact on Water Pollution. *Int. J. Environ. Res. Public Health* **2022**, *19*, 7437. [CrossRef] [PubMed]
25. Zhang, Y.; Granger, S.J.; Semenov, M.A.; Upadhayay, H.R.; Collins, A.L. Diffuse water pollution during recent extreme wet-weather in the UK: Environmental damage costs and insight into the future? *J. Clean. Prod.* **2022**, *338*, 130633. [CrossRef] [PubMed]

26. Naik, M.R.; Barik, M.; Prasad, K.V.; Kumar, A.; Verma, A.K.; Sahoo, S.K.; Jha, V.; Sahoo, N.K. Hydro-geochemical analysis based on entropy and geostatistics model for delineation of anthropogenic ground water pollution for health risks assessment of Dhenkanal district, India. *Ecotoxicology* **2022**, *31*, 549–564. [CrossRef]
27. Cordoba, A.; Saldias, C.; Urzúa, M.; Montalti, M.; Guernelli, M.; Focarete, M.L.; Leiva, A. On the Versatile Role of Electrospun Polymer Nanofibers as Photocatalytic Hybrid Materials Applied to Contaminated Water Remediation: A Brief Review. *Nanomaterials* **2022**, *12*, 756. [CrossRef]
28. Teng, Y.; Wang, Y.; Shi, B.; Fan, W.; Li, Z.; Chen, Y. Facile fabrication of superhydrophobic paper with durability, chemical stability and self-cleaning by roll coating with modified nano-TiO_2. *Appl. Nanosci.* **2020**, *10*, 4063–4073. [CrossRef]
29. Akbari, R.; Godeau, G.; Mohammadizadeh, M.; Guittard, F.; Darmanin, T. The influence of bath temperature on the one-step electrodeposition of non-wetting copper oxide coatings. *Appl. Surf. Sci.* **2020**, *503*, 144094. [CrossRef]
30. Cooney, R.; Wan, A.H.; O'Donncha, F.; Clifford, E. Designing environmentally efficient aquafeeds through the use of multicriteria decision support tools. *Curr. Opin. Environ. Sci. Health* **2021**, *23*, 100276. [CrossRef]
31. Li, Z.; Jiang, W.; Huang, J.; Wang, Y.; Guo, H. ZnO Promoted Persulfate Activation in Discharge Plasma System for Ofloxacin Degradation. *Catalysts* **2023**, *13*, 847. [CrossRef]
32. Lopes, O.F.; Paris, E.C.; Ribeiro, C. Synthesis of Nb_2O_5 nanoparticles through the oxidant peroxide method applied to organic pollutant photodegradation: A mechanistic study. *Appl. Catal. B Environ.* **2014**, *144*, 800–808. [CrossRef]
33. Batista, L.M.B.; Dos Santos, A.J.; da Silva, D.R.; de Melo Alves, A.P.; Garcia-Segura, S.; Martínez-Huitle, C.A. Solar photocatalytic application of NbO_2OH as alternative photocatalyst for water treatment. *Sci. Total Environ.* **2017**, *596*, 79–86. [CrossRef]
34. Dos Santos, A.J.; Batista, L.M.B.; Martínez-Huitle, C.A.; Alves, A.P.D.M.; Garcia-Segura, S. Niobium oxide catalysts as emerging material for textile wastewater reuse: Photocatalytic decolorization of azo dyes. *Catalysts* **2019**, *9*, 1070. [CrossRef]
35. Wang, H.; Wu, H.; Pang, H.; Xiong, Y.; Ma, S.; Duan, Y.; Hou, Y.; Mao, C. Lightweight PPy aerogel adopted with Co and SiO_2 nanoparticles for enhanced electromagnetic wave absorption. *J. Mater. Sci. Technol.* **2022**, *97*, 213–222. [CrossRef]
36. Sharma, P.; Prakash, J.; Palai, T.; Kaushal, R. Surface functionalization of bamboo leave mediated synthesized SiO_2 nanoparticles: Study of adsorption mechanism, isotherms and enhanced adsorption capacity for removal of Cr (VI) from aqueous solution. *Environ. Res.* **2022**, *214*, 113761. [CrossRef]
37. Alqahtani, M.J.; Mostafa, S.A.; Hussein, I.A.; Elhawary, S.; Mokhtar, F.A.; Albogami, S.; Tomczyk, M.; Batiha, G.E.-S.; Negm, W.A. Metabolic Profiling of *Jasminum grandiflorum* L. Flowers and Protective Role against Cisplatin-Induced Nephrotoxicity: Network Pharmacology and In Vivo Validation. *Metabolites* **2022**, *12*, 792. [CrossRef]
38. Mansour, K.A.; El-Neketi, M.; Lahloub, M.F.; Elbermawi, A. Nanoemulsions of *Jasminum humile* L. and *Jasminum grandiflorum* L. essential oils: An approach to enhance their cytotoxic and antiviral effects. *Molecules* **2022**, *27*, 3639. [CrossRef]
39. Sun, L.; Zhang, Y.; Wen, S.; Li, Q.; Chen, R.; Lai, X.; Zhang, Z.; Zhou, Z.; Xie, Y.; Zheng, X.; et al. Extract of *Jasminum grandiflorum* L. alleviates CCl_4-induced liver injury by decreasing inflammation, oxidative stress and hepatic CYP2E1 expression in mice. *Biomed. Pharmacother.* **2022**, *152*, 113255. [CrossRef]
40. Mansour, K.A.; Elbermawi, A.; Al-Karmalawy, A.A.; Lahloub, M.F.; El-Neketi, M. Cytotoxic effects of extracts obtained from plants of the Oleaceae family: Bio-guided isolation and molecular docking of new secoiridoids from *Jasminum humile*. *Pharm. Biol.* **2022**, *60*, 1374–1383. [CrossRef]
41. Sharmila, M.; Mani, R.J.; Parvathiraja, C.; Kader, S.M.A.; Siddiqui, M.R.; Wabaidur, S.M.; Islam, M.A.; Lai, W.C. Photocatalytic Dye Degradation and Bio-Insights of Honey-Produced α-Fe_2O_3 Nanoparticles. *Water* **2022**, *14*, 2301. [CrossRef]
42. Parvathiraja, C.; Katheria, S.; Siddiqui, M.R.; Wabaidur, S.M.; Islam, M.A.; Lai, W.C. Activated Carbon-Loaded Titanium Dioxide Nanoparticles and Their Photocatalytic and Antibacterial Investigations. *Catalysts* **2022**, *12*, 834. [CrossRef]
43. Jirovetz, L.; Buchbauer, G.; Schweiger, T.; Denkova, Z.; Slavchev, A.; Stoyanova, A.; Schmidt, E.; Geissler, M. Chemical composition, olfactory evaluation and antimicrobial activities of *Jasminum grandiflorum* L. absolute from India. *Nat. Prod. Commun.* **2007**, *2*, 1934578X0700200411. [CrossRef]
44. Zhao, G.; Yin, Z.; Dong, J. Antiviral efficacy against hepatitis B virus replication of oleuropein isolated from *Jasminum officinale* L. var. *grandiflorum*. *J. Ethnopharmacol.* **2009**, *125*, 265–268. [CrossRef]
45. Parlinska-Wojtan, M.; Depciuch, J.; Fryc, B.; Kus-Liskiewicz, M. Green synthesis and antibacterial effects of aqueous colloidal solutions of silver nanoparticles using clove eugenol. *Appl. Organomet. Chem.* **2018**, *32*, e4276. [CrossRef]
46. Amritphale, S.S.; Mishra, D.; Mudgal, M.; Chouhan, R.K.; Chandra, N. A novel green approach for making hybrid inorganic-organic geopolymeric cementitious material utilizing fly ash and rice husk. *J. Environ. Chem. Eng.* **2016**, *4*, 3856–3865. [CrossRef]
47. Da Silva, V.J.; de Almeida, E.P.; Gonçalves, W.P.; da Nóbrega, R.B.; de Araújo Neves, G.; de Lucena Lira, H.; Menezes, R.R.; de Lima Santana, L.N. Mineralogical and dielectric properties of mullite and cordierite ceramics produced using wastes. *Ceram. Int.* **2019**, *45*, 4692–4699. [CrossRef]
48. Gonçalves, W.P.; Silva, V.J.; Menezes, R.R.; Neves, G.A.; Lira, H.L.; Santana, L.N. Microstructural, physical and mechanical behavior of pastes containing clays and alumina waste. *Appl. Clay Sci.* **2017**, *137*, 259–265. [CrossRef]
49. Basak, M.; Rahman, M.L.; Ahmed, M.F.; Biswas, B.; Sharmin, N. The use of X-ray diffraction peak profile analysis to determine the structural parameters of cobalt ferrite nanoparticles using Debye-Scherrer, Williamson-Hall, Halder-Wagner and Size-strain plot: Different precipitating agent approach. *J. Alloys Compd.* **2022**, *895*, 162694. [CrossRef]

50. Selvanayaki, R.; Rameshbabu, M.; Muthupandi, S.; Razia, M.; Florence, S.S.; Ravichandran, K.; Prabha, K. Structural, optical and electrical conductivity studies of pure and Fe doped ZincOxide (ZnO) nanoparticles. *Mater. Today Proc.* **2022**, *49*, 2628–2631. [CrossRef]
51. Dong, R.; Wang, L.; Zhu, J.; Liu, L.; Qian, Y. A novel SiO_2–GO/acrylic resin nanocomposite: Fabrication, characterization and properties. *Appl. Phys. A* **2019**, *125*, 551. [CrossRef]
52. Bogart, K.H.A.; Dalleska, N.F.; Bogart, G.R.; Fisher, E.R. Plasma enhanced chemical vapor deposition of SiO_2 using novel alkoxysilane precursors. *J. Vac. Sci. Technol. A Vac. Surf. Film.* **1995**, *13*, 476–480. [CrossRef]
53. Tran, T.N.; Pham, T.V.A.; Le, M.L.P.; Nguyen, T.P.T. Synthesis of amorphous silica and sulfonic acid functionalized silica used as reinforced phase for polymer electrolyte membrane. *Adv. Nat. Sci. Nanosci. Nanotechnol.* **2013**, *4*, 045007. [CrossRef]
54. Sankareswaran, M.; Vanitha, M.; Periakaruppan, R.; Anbukumaran, A. *Phyllanthus emblica* mediated silica nanomaterials: Biosynthesis, structural and stability analysis. *Silicon* **2022**, *14*, 10123–10127. [CrossRef]
55. Ulfa, M.; Prasetyoko, D.; Trisunaryanti, W.; Bahruji, H.; Fadila, Z.A.; Sholeha, N.A. The effect of gelatin as pore expander in green synthesis mesoporous silica for methylene blue adsorption. *Sci. Rep.* **2022**, *12*, 15271. [CrossRef]
56. Salimi, E.; Nigje, A.K. Investigating the antibacterial activity of carboxymethyl cellulose films treated with novel Ag@ GO decorated SiO_2 nanohybrids. *Carbohydr. Polym.* **2022**, *298*, 120077. [CrossRef]
57. Madani, M.; Mansourian, M.; Almadari, S.; Mirzaee, O.; Tafreshi, M.J. Enhanced photosensitivity of heterostructure SiO_2/Bi_2WO_6/GO composite nanoparticles. *Phys. B Condens. Matter* **2022**, *645*, 414241. [CrossRef]
58. Nikpassand, M.; Fekri, L.Z.; Varma, R.S.; Hassanzadi, L.; Pashaki, F.S. Green synthesis of novel 5-amino-bispyrazole-4-carbonitriles using a recyclable Fe_3O_4@SiO_2@vanillin@thioglycolic acid nano-catalyst. *RSC Adv.* **2022**, *12*, 834–844. [CrossRef]
59. Calderón-Jiménez, B.; Montoro Bustos, A.R.; Pereira Reyes, R.; Paniagua, S.A.; Vega-Baudrit, J.R. Novel pathway for the sonochemical synthesis of silver nanoparticles with near-spherical shape and high stability in aqueous media. *Sci. Rep.* **2022**, *12*, 882. [CrossRef]
60. Barnawi, N.; Allehyani, S.; Seoudi, R. Biosynthesis and characterization of gold nanoparticles and its application in eliminating nickel from water. *J. Mater. Res. Technol.* **2022**, *17*, 537–545. [CrossRef]
61. Borzęcka, W.; Pereira, P.M.; Fernandes, R.; Trindade, T.; Torres, T.; Tomé, J.P. Spherical and rod shaped mesoporous silica nanoparticles for cancer-targeted and photosensitizer delivery in photodynamic therapy. *J. Mater. Chem. B* **2022**, *10*, 3248–3259. [CrossRef]
62. Rybin, M.V.; Sinelnik, A.D.; Tajik, M.; Milichko, V.A.; Ubyivovk, E.V.; Yakovlev, S.A.; Pevtsov, A.B.; Yavsin, D.A.; Zuev, D.A.; Makarov, S.V. Optically Reconfigurable Spherical Ge-Sb-Te Nanoparticles with Reversible Switching. *Laser Photonics Rev.* **2022**, *16*, 2100253. [CrossRef]
63. Arif, M.; Kumam, P.; Kumam, W.; Mostafa, Z. Heat transfer analysis of radiator using different shaped nanoparticles water-based ternary hybrid nanofluid with applications: A fractional model. *Case Stud. Therm. Eng.* **2022**, *31*, 101837. [CrossRef]
64. Zonarsaghar, A.; Mousavi-Kamazani, M.; Zinatloo-Ajabshir, S. Sonochemical synthesis of CeVO4 nanoparticles for electrochemical hydrogen storage. *Int. J. Hydrogen Energy* **2022**, *47*, 5403–5417. [CrossRef]
65. Behzadnia, H.; Jin, H.; Najafian, M.; Hatami, M. Investigation of super-critical water-based nanofluid with different nanoparticles (shapes and types) used in the rectangular corrugated tube of reactors. *Alex. Eng. J.* **2022**, *61*, 2330–2347. [CrossRef]
66. Sakata, T.; Ogawa, S.; Inoue, K.; Shimizu, Y.; Tanahashi, Y. Effects of post-deposition annealing on chemical composition of SiN_x film in $SiO_2/SiN_x/SiO_2$/Si stacked structure. *Surf. Interface Anal.* **2022**, *54*, 661–666. [CrossRef]
67. Arellano-Galindo, L.G.; Reynosa-Martínez, A.C.; Gaitán-Arévalo, J.R.; Valerio-Rodríguez, M.F.; Vargas-Gutiérrez, G.; López-Honorato, E. Superhydrophobic to superhydrophilic wettability transition of functionalized SiO_2 nanoparticles. *Ceram. Int.* **2022**, *48*, 21631–21637. [CrossRef]
68. Wang, L.; Zhang, J.; Zhang, Y.; Yu, H.; Qu, Y.; Yu, J. Inorganic Metal-Oxide Photocatalyst for H_2O_2 Production. *Small* **2022**, *18*, 2104561. [CrossRef]
69. Alaghmandfard, A.; Ghandi, K. A Comprehensive Review of Graphitic Carbon Nitride (g-C3N4)–Metal Oxide-Based Nanocomposites: Potential for Photocatalysis and Sensing. *Nanomaterials* **2022**, *12*, 294. [CrossRef]
70. Soni, V.; Singh, P.; Khan, A.A.P.; Singh, A.; Nadda, A.K.; Hussain, C.M.; Van Le, Q.; Rizevsky, S.; Nguyen, V.H.; Raizada, P. Photocatalytic transition-metal-oxides-based p–n heterojunction materials: Synthesis, sustainable energy and environmental applications, and perspectives. *J. Nanostruct. Chem.* **2023**, *13*, 129–166. [CrossRef]
71. Dong, X.; Li, Y.; Li, D.; Liao, D.; Qin, T.; Prakash, O.; Kumar, A.; Liu, J. A new 3D 8-connected Cd (ii) MOF as a potent photocatalyst for oxytetracycline antibiotic degradation. *CrystEngComm* **2022**, *24*, 6933–6943. [CrossRef]
72. Rao, C.; Zhou, L.; Pan, Y.; Lu, C.; Qin, X.; Sakiyama, H.; Muddassir, M.; Liu, J. The extra-large calixarene-based MOFs-derived hierarchical composites for photocatalysis of dye: Facile syntheses and contribution of carbon species. *J. Alloys Compd.* **2022**, *897*, 163178. [CrossRef]
73. Wang, J.; Rao, C.; Lu, L.; Zhang, S.; Muddassir, M.; Liu, J. Efficient photocatalytic degradation of methyl violet using two new 3D MOFs directed by different carboxylate spacers. *CrystEngComm* **2021**, *23*, 741–747. [CrossRef]
74. Li, Q.; Wei, G.; Duan, G.; Zhang, L.; Li, Z.; Wei, Z.; Zhou, Q.; Pei, R. Photocatalysis activation of peroxydisulfate over oxygen vacancies-rich mixed metal oxide derived from red mud-based layered double hydroxide for ciprofloxacin degradation. *Sep. Purif. Technol.* **2022**, *289*, 120733. [CrossRef]

75. Chuaicham, C.; Inoue, T.; Balakumar, V.; Tian, Q.; Sasaki, K. Fabrication of visible-light-active ZnCr mixed metal oxide/fly ash for photocatalytic activity toward pharmaceutical waste ciprofloxacin. *J. Ind. Eng. Chem.* **2022**, *108*, 263–273. [CrossRef]
76. Govindhan, P.; Pragathiswaran, C. Silver nanoparticle decorated on ZnO@SiO_2 nanocomposite and application for photocatalytic dye degradation of methylene blue. *Natl. Acad. Sci. Lett.* **2019**, *42*, 323–326. [CrossRef]
77. Govindhan, P.; Pragathiswaran, C. Synthesis and characterization of TiO_2@SiO_2–Ag nanocomposites towards photocatalytic degradation of rhodamine B and methylene blue. *J. Mater. Sci. Mater. Electron.* **2016**, *27*, 8778–8785. [CrossRef]
78. Arshad, A.; Iqbal, J.; Mansoor, Q.; Ahmed, I. Graphene/SiO_2 nanocomposites: The enhancement of photocatalytic and biomedical activity of SiO_2 nanoparticles by graphene. *J. Appl. Phys.* **2017**, *121*, 244901. [CrossRef]
79. Kim, C.; Choi, M.; Jang, J. Nitrogen-doped SiO_2/TiO_2 core/shell nanoparticles as highly efficient visible light photocatalyst. *Catal. Commun.* **2010**, *11*, 378–382. [CrossRef]
80. Arshad, M.; Qayyum, A.; Shar, G.A.; Soomro, G.A.; Nazir, A.; Munir, B.; Iqbal, M. Zn-doped SiO_2 nanoparticles preparation and characterization under the effect of various solvents: Antibacterial, antifungal and photocatlytic performance evaluation. *J. Photochem. Photobiol. B Biol.* **2018**, *185*, 176–183. [CrossRef]
81. Rani, N.; Ahlawat, R.; Goswami, B. Annealing effect on bandgap energy and photocatalytic properties of CeO_2–SiO_2 nanocomposite prepared by sol-gel technique. *Mater. Chem. Phys.* **2020**, *241*, 122401. [CrossRef]
82. Zhao, W.; Feng, L.; Yang, R.; Zheng, J.; Li, X. Synthesis, characterization, and photocatalytic properties of Ag modified hollow SiO_2/TiO_2 hybrid microspheres. *Appl. Catal. B Environ.* **2011**, *103*, 181–189. [CrossRef]
83. Sarani, M.; Joshaghani, A.B.; Najafidoust, A.; Asl, E.A.; Hakki, H.K.; Bananifard, H.; Sillanpaa, M. Sun-light driven photo degradation of organic dyes from wastewater on precipitation Ag_2CrO_4 over SiO_2-aerogel and nano silica. *Inorg. Chem. Commun.* **2021**, *133*, 108877. [CrossRef]
84. Zhou, X.; Zhang, G.; Shao, C.; Li, X.; Jiang, X.; Liu, Y. Fabrication of g-C_3N_4/SiO_2-Au composite nanofibers with enhanced visible photocatalytic activity. *Ceram. Int.* **2017**, *43*, 15699–15707. [CrossRef]
85. Hu, C.; Tang, Y.; Jimmy, C.Y.; Wong, P.K. Photocatalytic degradation of cationic blue X-GRL adsorbed on TiO_2/SiO_2 photocatalyst. *Appl. Catal. B Environ.* **2003**, *40*, 131–140. [CrossRef]
86. Li, X.; Ye, J. Photocatalytic degradation of rhodamine B over $Pb_3Nb_4O_{13}$/fumed SiO_2 composite under visible light irradiation. *J. Phys. Chem. C* **2007**, *111*, 13109–13116. [CrossRef]
87. Zinatloo-Ajabshir, S.; Mortazavi-Derazkola, S.; Salavati-Niasari, M. Nd_2O_3-SiO_2 nanocomposites: A simple sonochemical preparation, characterization and photocatalytic activity. *Ultrason. Sonochem.* **2018**, *42*, 171–182. [CrossRef]
88. Wu, L.; Zhou, Y.; Nie, W.; Song, L.; Chen, P. Synthesis of highly monodispersed teardrop-shaped core–shell SiO_2/TiO_2 nanoparticles and their photocatalytic activities. *Appl. Surf. Sci.* **2015**, *351*, 320–326. [CrossRef]
89. Alavi, M. Bacteria and fungi as major bio-sources to fabricate silver nanoparticles with antibacterial activities. *Expert Rev. Anti-Infect. Ther.* **2022**, *20*, 897–906. [CrossRef]
90. Franco, D.; Calabrese, G.; Guglielmino, S.P.P.; Conoci, S. Metal-Based Nanoparticles: Antibacterial Mechanisms and Biomedical Application. *Microorganisms* **2022**, *10*, 1778. [CrossRef]
91. Nivetha, A.; Prabha, I. Surfactant-Enhanced Nano Spinel Oxide for Applications in Catalysis, Dye Degradation and Antibacterial Activity. *ChemistrySelect* **2022**, *7*, e202202389. [CrossRef]
92. Al-Mushki, A.A.; Ahmed, A.A.A.; Abdulwahab, A.M.; Al-Asbahi, B.A.; Abduljalil, J.; Saad, F.A.; Al-Hada, N.M.; Qaid, S.M.; Ghaithan, H.M. Structural, optical, and antibacterial characteristics of mixed metal oxide CdO–NiO–Fe_2O_3 nanocomposites prepared using a self-combustion method at different polyvinyl alcohol concentrations. *Appl. Phys. A* **2022**, *128*, 279. [CrossRef]
93. Prisrin, S.A.; Priyanga, M.; Ponvel, K.M.; Kaviarasan, K.; Kalidass, S. Plant Mediated Approach for the Fabrication of Nano CuO–NiO Mixed Oxides Using Aqueous Extract of Mimusops Elengi Leaf: Green Synthesis, Characterization and Antibacterial Activity Studies. *J. Clust. Sci.* **2022**, *33*, 765–772. [CrossRef]
94. Matalkeh, M.; Nasrallah, G.K.; Shurrab, F.M.; Al-Absi, E.S.; Mohammed, W.; Elzatahry, A.; Saoud, K.M. Visible light photocatalytic activity of Ag/WO_3 nanoparticles and its antibacterial activity under ambient light and in the dark. *Results Eng.* **2022**, *13*, 100313. [CrossRef]
95. Clinical and Laboratory Standards Institute (CLSI). *Performance Standards for Antimicrobial Disk Susceptibility Tests*, 11th ed.; Approved Standard M02-A11; Clinical and Laboratory Standards Institute: Wayne, PA, USA, 2012; Volume 32, pp. 11–13.
96. Dolgov, A.; Lopaev, D.; Lee, C.J.; Zoethout, E.; Medvedev, V.; Yakushev, O.; Bijkerk, F. Characterization of carbon contamination under ion and hot atom bombardment in a tin-plasma extreme ultraviolet light source. *Appl. Surf. Sci.* **2015**, *353*, 708–713. [CrossRef]